



Contents lists available at ScienceDirect

Journal of Sound and Vibration

journal homepage: www.elsevier.com/locate/jsvi



Arbitrary scattering of an acoustical Bessel beam by a rigid spheroid with large aspect-ratio



Zhixiong Gong^a, Wei Li^{a,b,c,*}, Farid G. Mitri^d, Yingbin Chai^a, Yao Zhao^{a,b,c}

^a School of Naval Architecture and Ocean Engineering, Huazhong University of Science and Technology, Wuhan 430074, PR China

^b Hubei Key Laboratory of Naval Architecture and Ocean Engineering Hydrodynamics (HUST), Wuhan 430074, PR China

^c Collaborative Innovation Center for Advanced Ship and Deep-Sea Exploration (CISSE), Shanghai 200240, PR China

^d Chevron, Area 52 Technology-ETC, Santa Fe, NM 87508, USA

ARTICLE INFO

Article history:

Received 1 February 2016

Received in revised form

27 July 2016

Accepted 3 August 2016

Handling Editor: Y. Auregan

Available online 18 August 2016

Keywords:

Bessel beam

T-matrix method

Large-aspect-ratio rigid spheroid

Franz wave

ABSTRACT

In this paper, the *T*-matrix (null-field) method is applied to investigate the acoustic scattering by a large-aspect-ratio rigid spheroid immersed in a non-viscous fluid under the illumination of an unbounded zeroth-order Bessel beam with arbitrary orientation. Based on the proposed method, a MATLAB software package is constructed accordingly, and then verified and validated to compute the acoustic scattering by a rigid oblate or prolate spheroid in the Bessel beam. Several numerical examples are carried out to investigate the novel phenomenon of acoustic scattering by spheroids in Bessel beams with arbitrary incidence, with particular emphasis on the aspect ratio (i.e. the ratio of the polar radius over the equatorial radius of the spheroid), the half-cone angle of Bessel beam, the dimensionless frequency, as well as the angle of incidence. The quasi-periodic oscillations are observed in the plots of the far-field backscattering form function modulus versus the dimensionless frequency, owing to the interference between the specular reflection and the Franz wave circumnavigating the spheroid in the surrounding fluid. Furthermore, the 3D far-field scattering directivity patterns at end-on incidence and 2D polar plots at arbitrary angles of incidence are exhibited, which could provide new insights into the physical mechanisms of Bessel beam scattering by flat or elongated spheroid. This research work may provide an impetus for the application of acoustic Bessel beam in engineering practices.

© 2016 Elsevier Ltd. All rights reserved.

1. Introduction

During the past few decades, investigations dealing with Bessel beams have attracted more and more attention in the fields of optics [1–5], electromagnetics [6–8] and acoustics [9–12] ever since they were introduced through theoretical and experimental investigations [13,14]. Hsu successfully produced a Bessel beam transducer by polarizing a piezoelectric ceramic disk nonuniformly [15], which provides great impetus for researchers to further explore its novel beam-forming and wave propagation properties. As is known to all, Bessel beams have been demonstrated to have several advantages over infinite plane waves and Gaussian beams, because they can propagate without distortion over a characteristic distance in free space. In addition, a Bessel beam is characterized by two important features, namely, the nondiffraction property and

* Corresponding author at: School of Naval Architecture and Ocean Engineering, Huazhong University of Science and Technology, Wuhan 430074, China.
E-mail address: hustliw@hust.edu.cn (W. Li).

self-construction ability. The former feature means that the transverse intensity profile in the plane perpendicular to the direction of Bessel beam axis remains unaltered [14,16–18], while the second one describes the ability of the Bessel beam to reconstruct its initial intensity profile after encountering an obstacle in the case where the incident waves (forming the beam) are not blocked completely [19–21]. Owing to the superior characteristics mentioned above, acoustical Bessel beams have continued to receive increasing interest and many researchers have been devoting their efforts to study physical phenomena involving Bessel beams both theoretically and experimentally.

Recently, many studies have been carried out on the acoustic scattering of a Bessel beam interacting with rigid, soft and elastic targets. Axial radiation force of a Bessel beam on a sphere (including rigid, fluid and elastic solids spheres) was initially studied by Marston and negative (pulling) axial forces were found under certain conditions which may provide an impetus to design acoustic tweezers [9] and tractor beams [22]. After that, Marston further investigated the monostatic and bistatic (i.e. polar) scattering characteristics of both rigid and soft spheres centered on a zeroth-order [23] or high-order [22] Bessel beam. Later, the resonance scattering of an elastic solid sphere and spherical shell under the Bessel beam illumination, and influences of several selective half-cone angles on the suppression of backscattering resonance were reported in detail [24]. Subsequently, researches involving the acoustic scattering of Bessel beams were further developed by others, such as Mitri and Li's group. There has been considerable interest in Mitri's study of high-order Bessel beams to explore acoustic scattering characteristics by several objects, including rigid (movable and immovable) spheres [25–27], elastic spheres [10,28], elastic spherical shells [29,30] and rigid spheroids [31,32]. In addition, Mitri devoted much effort to further investigate the acoustic radiation force exerted by Bessel beams on spheres [33–36], and rigid spheroids [37,38] based on a far-field scattering approach [39]. Similarly, our research group has studied the scattering problems of arbitrary-shape rigid scatterers facing the incident Bessel beam [40]. In our work, the backscattering fields of rigid spheroid and finite cylinder with two hemispherical endcaps were investigated, and the peak-to-peak intervals in backscattering form functions were analyzed with both geometric and numerical method.

However, as reviewed above, most of the computations associated with Bessel beam scattering have concentrated on objects with spherical geometry. Only few works [31,32,37,38] were aimed to explore the new physical phenomena of acoustical scattering of Bessel beam from nonspherical rigid obstacles by using the partial-wave series expansion (PWSE) method in spherical coordinates. However, the PWSE method suffers an ill-conditioning during matrix inversion procedures so it has the restrictions that the aspect ratio of rigid spheroid is generally smaller than 3:1. To the authors' knowledge, it still remains unpublished to calculate the acoustic scattering of a Bessel beam by a spheroid with a large aspect-ratio reaching 10:1, both in normal and oblique incidence cases. It is of some importance to study the highly elongated or extremely flat rigid spheroids which can be found in many theoretical models in fluid dynamics and engineering applications. For instance, in resonance scattering theory (RST), the scattering fields by rigid targets are always taken as non-resonant backgrounds for elastic solid and thick shell structures [41]. On this basis, it is possible to isolate the "pure" elastic resonance scattering from the total scattering fields by subtracting a corresponding rigid background for targets with spheroidal geometries, which plays an important role in the field of detection and recognition of submerged elongated targets. In the literature reported in the past, a number of computational techniques were developed to explore acoustic scattering problems by a rigid spheroid under the plane wave incidence, including the separation of variables methods in spheroidal coordinates [42,43], the iterative extended boundary condition method (IEBCM) [44,45], the finite difference time-domain method [46], the finite element method (FEM) [47], and the shape perturbation method [48], to name but a few. However, the above techniques are somewhat subjected to their own weaknesses and applicable circumstances [49].

In the present work, the T -matrix method (also called the null-field method, or extended boundary condition method EBCM) is initially extended to compute acoustic scattering by a large aspect-ratio rigid spheroid interacting with an acoustical Bessel beam at arbitrary incidence, with no restriction to the on-axis case treated previously [32]. The T -matrix method, as originally conceived by Waterman [50,51], has been demonstrated to be a powerful tool to handle acoustic scattering problems for nonspherical targets, such as elliptic cylinders [52,53], spheroids [54–58] and even the combination of them [59]. The advantage of the T -matrix method is to expand all field quantities in terms of a set of spherical functions, which is much convenient from a computational standpoint. The main point of the present method is to obtain the T matrix (transition matrix) that gives a direct relationship between the known expansion coefficients of the incident waves and the unknown expansion coefficients of the scattered field. Moreover, the T -matrix formulation allows the computation of scattering problems at a variety of incidence and scattering angles. Therefore, it is anticipated that several novel physical phenomena occurring during the interaction of an acoustical Bessel beam with a large aspect-ratio rigid spheroid with arbitrary orientation may be discovered by numerical computations using this method.

The frame of this article is outlined as follows. In the first part of Section 2, theoretical formulas of the T -matrix method for the acoustic scattering by rigid (oblate and prolate) spheroid immersed in fluid are presented briefly. Subsequently, the expansion coefficients of the incident Bessel beam are derived in detail in the second part of Section 2. In Section 3, numerical validation is firstly implemented to verify the correctness of the T -matrix approach for large aspect-ratio rigid spheroids. Then, additional numerical examples are carried out with particular emphasis on the aspect ratio, the half-cone angles, the dimensionless frequency, as well as the incidence angles of the Bessel beam. Finally, some useful concluding remarks are summarized in Section 4.

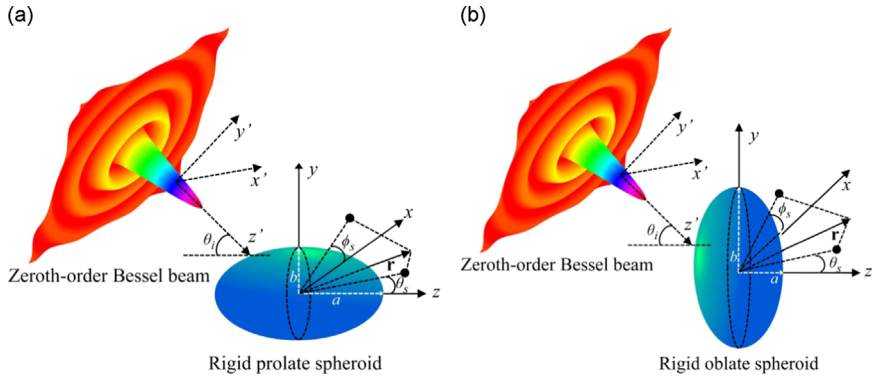


Fig. 1. The schematic of a monochromatic zeroth-order Bessel beam interacting with a rigid spheroid at arbitrary angles of incidence θ_i in a spherical coordinates system. Panel (a) corresponds to a rigid prolate spheroid with polar radius greater than equatorial radius $a > b$, while panel (b) corresponds to the rigid oblate spheroid with a polar radius less than the equatorial radius $a < b$.

2. Theoretical method

In this section, the necessary formulas of T -matrix method for acoustic scattering by a rigid spheroid immersed in fluid under Bessel wave incidence are presented. In addition, the detailed procedure for deriving the expansion coefficients for an incident unbounded zeroth-order Bessel beam is also provided in the following part.

2.1. T -matrix method for a rigid spheroid in a non-viscous fluid

Consider a rigid (prolate or oblate) spheroid with a polar radius a and an equatorial radius b immersed in an infinite, homogeneous and nonviscous fluid. The (prolate or oblate) spheroid is illuminated by an acoustic monochromatic zeroth-order Bessel beam at an arbitrary angle of incidence, as shown in Fig. 1. The ideal fluid surrounding the spheroid has a sound velocity c and a density ρ . For convenience, the time factor $\exp(-i\omega t)$ is suppressed throughout since all fields have the same harmonic time-dependence.

The total velocity potential $\phi(\mathbf{r})$ in fluid is written as the sum of the incident ($\phi^i(\mathbf{r})$) and the scattered ($\phi^s(\mathbf{r})$) velocity potentials:

$$\phi(\mathbf{r}) = \phi^i(\mathbf{r}) + \phi^s(\mathbf{r}) \quad (1)$$

Note that all the above velocity potentials satisfy the Helmholtz equation which can be expressed as

$$(\nabla^2 + k^2) \begin{pmatrix} \phi(\mathbf{r}) \\ \phi^i(\mathbf{r}) \\ \phi^s(\mathbf{r}) \end{pmatrix} = 0 \quad (2)$$

where $k = \omega/c$ is the wave number in the surrounding fluid. In the following, the integral representation and the null field equation, which are originally presented in Waterman's paper on the T-matrix formulation of acoustic wave scattering [60], are given by

$$\phi^i(\mathbf{r}) + \int_S \left[\phi_+ \vec{\mathbf{n}} \cdot \nabla g(\mathbf{r}, \mathbf{r}') - (\vec{\mathbf{n}} \cdot \nabla_+ \phi) g(\mathbf{r}, \mathbf{r}') \right] dS = \begin{cases} \phi(\mathbf{r}) & \mathbf{r} \text{ outside } S \\ 0 & \mathbf{r} \text{ inside } S \end{cases} \quad (3)$$

where

$$g(\mathbf{r}, \mathbf{r}') = \exp(ik|\mathbf{r} - \mathbf{r}'|)/(k|\mathbf{r} - \mathbf{r}'|) \quad (4)$$

is the free space Green's function of the Helmholtz equation. S represents the surface of spheroid and $\vec{\mathbf{n}}$ is the unit normal taken as outward pointing. The quantities ϕ_+ and $\vec{\mathbf{n}} \cdot \nabla_+ \phi$ stand for the velocity potential and normal component of the velocity on the outside of S , respectively.

The spheroid considered in the present article is assumed to be perfectly rigid. Because of an azimuthal symmetry, the surface shape function of spheroid $S(\theta)$ is only dependent on the polar angle θ , with its representation as follow

$$S(\theta) = (\cos^2 \theta/a^2 + \sin^2 \theta/b^2)^{-1/2} \quad (5)$$

The parameter a denotes the polar radius, which is the length between the center and the endpoint of spheroid along its rotation axis of symmetry, while b is the equatorial radius. A prolate spheroid is defined when the polar radius is larger than the equatorial radius ($a > b$), depicted as Fig. 1(a), whereas an oblate spheroid is defined when $a < b$, depicted in Fig. 1(b).

Especially, in the case of $a = b$, the spheroid degenerates to a sphere, whose surface shape function $S(\theta)$ no longer depends on the polar angle θ .

For the perfectly rigid spheroid, the Neumann boundary condition is imposed on the surface of the spheroid at $\mathbf{r} = S(\theta)$, such that

$$\vec{\mathbf{n}} \cdot \nabla + \phi(\mathbf{r})|_{\mathbf{r}=S(\theta)} = 0 \quad (6)$$

In order to obtain the transition matrix for the rigid spheroid, all three fields in Eq. (2) and the Green's function should be expanded in terms of a set of spherical harmonic functions. To this end, the following scalar basis function is defined as

$$\phi_{nm\sigma}(\mathbf{r}) = \xi_{nm} h_n(kr) P_n^m(\cos \theta) \begin{cases} \cos(m\varphi), & \sigma = e \\ \sin(m\varphi), & \sigma = o \end{cases} \quad (7)$$

where,

$$\xi_{nm} = \left(\varepsilon_{nm} \frac{(2n+1)(n-m)!}{4\pi(n+m)!} \right)^{1/2} \quad (8)$$

and $h_n(kr)$ is the spherical Hankel function of the first kind, $P_n^m(\cos \theta)$ is the associated Legendre function and $\varepsilon_m = 2 - \delta_{m0}$ is the Neumann factor. $\sigma = e, o$ (even, odd) specifies the azimuthal parity, $m = 0, 1, \dots, n$ specifies the rank, and $n = 0, 1, \dots, \infty$ specifies the order of the spherical wave functions.

Due to the fact that the incident fields are finite at the origin, the spherical Hankel function of the first kind (which is singular at the origin) in Eq. (7) should be replaced by the spherical Bessel function of the first kind $j_n(kr)$ which is regular at the origin. Therefore, we can use the revised basis function, denoted by $\text{Re}\phi_{nm\sigma}$, to expand the incident field.

The velocity potentials of the incident and scattered fields can be expanded as

$$\phi^i(\mathbf{r}) = \sum_{n=0}^{\infty} \sum_{m=0}^n \sum_{\sigma} a_{nm\sigma} \text{Re}\phi_{nm\sigma}(\mathbf{r}) \quad (9)$$

$$\phi^s(\mathbf{r}) = \sum_{n=0}^{\infty} \sum_{m=0}^n \sum_{\sigma} f_{nm\sigma} \phi_{nm\sigma}(\mathbf{r}) \quad (10)$$

where $a_{nm\sigma}$ are the known coefficients of the incident Bessel beam (derived in detail below) and $f_{nm\sigma}$ are the unknown coefficients of the scattered fields, respectively. Note that the infinite summation in Eqs. (9) and (10) cannot be evaluated practically. Nevertheless, they can be numerically computed after adequate truncation at an appropriate limit n_{\max} . This limit should be judiciously chosen so that high precision and adequate convergence of the truncated series are warranted.

In addition, the Green's function $g(\mathbf{r}, \mathbf{r}')$ and the unknown surface field ϕ_+ are also expanded in the following forms

$$g(\mathbf{r}, \mathbf{r}') = ik \sum_n \sum_m \sum_{\sigma} \phi_{nm\sigma}(r_>) \text{Re}\phi_{nm\sigma}(r_<) \quad (11)$$

$$\phi_+(\mathbf{r}) = \sum_n \sum_m \sum_{\sigma} \alpha_{nm\sigma} \phi_{nm\sigma}(\mathbf{r}) \quad (12)$$

Here, all the formulas, including the integral representations, the rigid boundary condition and expansions of all fields and Green's function, are available, and hence the transition matrix can be derived immediately and given by Waterman in an obvious matrix notation as

$$f = Ta \quad (13)$$

where T is the transition matrix (T matrix) of rigid spheroid given by

$$T = -\text{Re}QQ^{-1} \quad (14)$$

The detailed expression of Q is given in [61,62], such that

$$\begin{aligned} Q_{nm,n'm'}^{\sigma\sigma'} &= \int_0^\pi \xi_{n'm} j_{n'}(kr) P_{n'}^{m'}(\cos \theta) \xi_{nm} \left[\frac{\partial h_n(kr)}{\partial r} P_n^m(\cos \theta) - \frac{r_\theta}{r^2} h_n(kr) \frac{\partial P_n^m(\cos \theta)}{\partial \theta} \right] \\ &\quad \times r^2 \sin \theta d\theta \int_0^{2\pi} \begin{pmatrix} \cos m'\varphi \\ \sin m'\varphi \end{pmatrix} \begin{pmatrix} \cos m\varphi \\ \sin m\varphi \end{pmatrix} d\varphi \end{aligned} \quad (15)$$

In particular, the transition matrix obtained is independent of incident fields and solely depends on the geometry of the scatterer and the corresponding boundary conditions at the interface.

2.2. Expansion coefficients of the incident Bessel beam

In this part, the expressions for the expansion coefficients $a_{nm\sigma}$ in the case of a zeroth-order Bessel beam are derived. It is possible to analyze the acoustic scattered fields using the T-matrix method as long as the expansion coefficients of the

incident Bessel beam are obtained. Our motivation is to expand the velocity potential of the zeroth-order Bessel beam into two parts in a product form, namely the revised basis function $\text{Re}\phi_{nm\sigma}(\mathbf{r})$ and the desired incident coefficients of Bessel beam $a_{nm\sigma}$.

The starting point of derivation begins with the complex velocity potential of an unbounded zero-order Bessel beam expressed as follows [23]

$$\phi_B(z, \rho) = \phi_0 \exp(i k Z) J_0(\mu \rho) \quad (16)$$

where ϕ_0 is the beam amplitude, z and ρ specify the axial and radial coordinates, k and μ , satisfying the relation $\kappa^2 + \mu^2 = k^2$, represent the axial and radial wavenumbers, and J_0 is a zeroth-order cylindrical Bessel function of the first kind.

Given by Eq. (B2) in Appendix B [23], Eq. (16) could be expanded in spherical coordinates (r, θ, φ) as

$$\phi_B(r, \theta) = \phi_0 \sum_{n=0}^{\infty} i^n \times (2n+1) j_n(kr) P_n(\cos \theta) P_n(\cos \beta) \quad (17)$$

where β denotes half-cone angle of the Bessel beam and θ is the polar angle. By using the addition theorem for the Legendre functions [63], the expression for $P_n(\cos \theta)$ becomes

$$P_n(\cos \theta) = \sum_{m=0}^n \epsilon_m \frac{(n-m)!}{(n+m)!} \times P_n^m(\cos \theta_i) P_n^m(\cos \theta_s) \cos m(\varphi_i - \varphi_s) \quad (18)$$

where θ_i and θ_s represent the incident and scattered axial angles, respectively.

Substituting Eqs. (7), (8), (18) into Eq. (17), the complex velocity potential of the zeroth-order Bessel beam is expressed according to a product form as

$$\phi_B(r, \theta) = a_{nm\sigma} \times \text{Re}\phi_{nm\sigma}(\mathbf{r}) \quad (19)$$

where $a_{nm\sigma}$ stands for the expansion coefficients of the incident unbounded zeroth-order Bessel beam given by

$$a_{nm\sigma} = 4\pi \xi_{nm} i^n \times P_n^m(\cos \theta_i) P_n^m(\cos \beta) \begin{cases} \cos(m\varphi_i), & \sigma = e \\ \sin(m\varphi_i), & \sigma = o \end{cases} \quad (20)$$

It should be noted that the expression of the expansion coefficients depends on the half-cone angle β , as well as the incident axial angles θ_i and azimuthal angles φ_i . The half-cone angle β is a characteristic parameter of Bessel beam, which is in fact the angle describing the plane wave vector component with respect to the beam axis. Particularly, when $\beta = 0$, the zeroth-order Bessel beam turns into an ordinary plane wave. The incident axial angle θ_i can vary from 0° to 360°.

After substituting Eq. (14) and the expansion coefficients for the incident Bessel beam given by Eq. (20) into the relationship according to Eq. (13), the corresponding scattered fields by a rigid spheroid under the illumination of an ideal zeroth-order Bessel beam can be acquired at once by Eq. (10). In this paper, the far-field form function f_∞ is introduced, which gives a dimensionless representation of the scattered pressure and is used extensively in the acoustic literature [64–66]. By analogy with the asymptotic scattering amplitude for the sphere case, the asymptotic expression of the far-field velocity potential for a rigid spheroid could be written in the form of f_∞ as

$$\lim_{r \rightarrow \infty} \phi^s = \phi_0 \frac{r_0}{2r} f_\infty(kr_0, \theta, \varphi, \beta) \exp(ikr) \quad (21)$$

where r_0 is the semi-major axis of the spheroid (the larger one between a and b), and r is the distance from the origin to the field point. It can be noted from Eq. (21) that for the Bessel beam cases, the form function is dependent on the dimensionless frequency, the parameters of the incident wave (including the incident angles and the half-cone angle), and the observation directions of the scattered fields.

3. Numerical results and discussions

In this section, several numerical examples are carried out to demonstrate the feasibility of utilizing the T -matrix method to compute the acoustic scattering of zeroth-order Bessel beam by rigid spheroids with large aspect ratios. A MATLAB software package is constructed based on the present theoretical method and utilized to calculate the monostatic and bistatic far-field form function modulus for a rigid oblate or prolate spheroid illuminated by an ideal zeroth-order Bessel beam, with particular emphasis on the aspect ratio a/b (=polar radius/equatorial radius), the half-cone angle β of Bessel beam, the dimensionless frequency, as well as the angle of incidence θ_i .

3.1. Numerical validation

To verify the accuracy of the theoretical formulas based on the T -matrix method presented in Section 2 for the Bessel beam, several numerical examples aiming to obtain the monostatic or bistatic far-field scattered fields were conducted, including the rigid prolate spheroids under end-on and oblique incidences and also the special case of a rigid sphere, either in the ordinary plane waves or Bessel beams. First of all, the stability issues of the T -matrix method for a rigid spheroid with

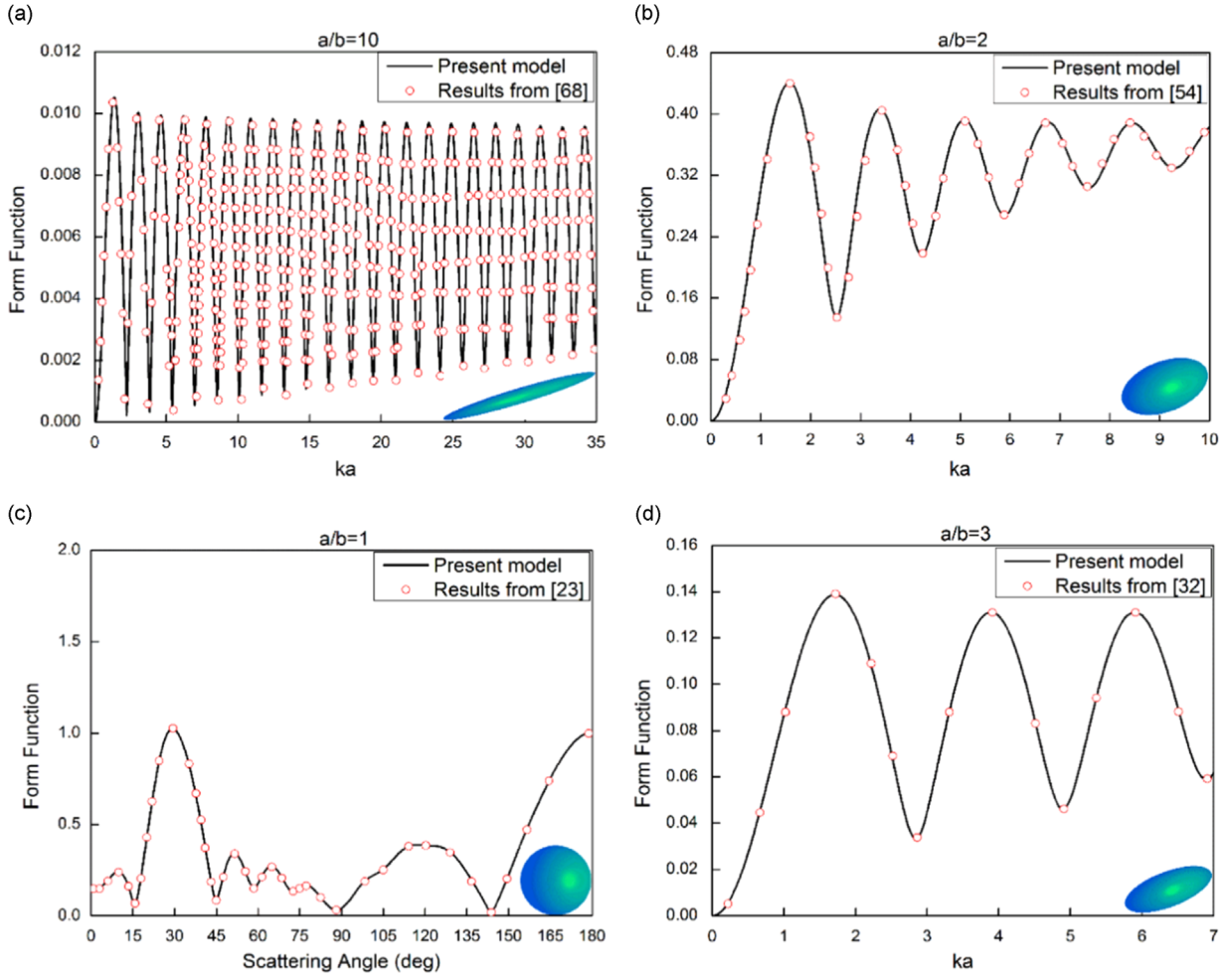


Fig. 2. The far-field backscattering form function modulus for a rigid immovable spheroid. Panels (a)–(b) are in plane wave illumination, while panels (c) and (d) are in the zeroth-order Bessel beams. Panels (a) corresponds to a highly elongated spheroid with an aspect ratio of $a/b = 10$ for end-on ($\theta_i = 0^\circ$) incidence, while panel (b) is for a spheroid with an aspect ratio of $a/b = 2$ at oblique incidence ($\theta_i = 45^\circ$). Panel (c) describes the bistatic scattering of a rigid sphere for Bessel beam illumination ($\beta = 30^\circ$). Panel (d) corresponds to a rigid spheroid with aspect ratio $a/b = 2$ and half-cone angle $\beta = 60^\circ$.

large aspect ratio will be discussed. As claimed in Mitri's work [31,32], the partial-wave series expansion method in spherical coordinates may fail to compute the acoustical Bessel beam scattering for highly elongated or highly flat geometries for the reason that the system of linear equations may become unsolvable because of an ill-conditioning during matrix inversion procedures. Similarly, it is essential to note that the T -matrix method with standard spherical formulation is not always stable for geometry with large aspect-ratio, because the elements of the Q matrix in Eq. (15) with $n > n'$ suffer from numerical cancellation noise when the surface integral is computed. Fortunately, as pointed out by Sarkissian et al. [59], the T -matrix method based on standard formulations can be performed stably at large aspect ratios for rigid spheroids because the matrix Q given in Eqs. (14) and (15) is symmetric in this case. Indeed, in our home-made MATLAB package software, only the elements in the Q matrix with $n < n'$, which can be integrated accurately are computed. The elements of Q with $n > n'$, which suffer from numerical cancellation noise when the surface integral is computed, are obtained by reflecting the elements with $n < n'$ across the diagonal. In consequence, the full Q matrix is obtained and the transition matrix can be computed stably. It is necessary to note that for rigid shapes with an asymmetric Q matrix, the stability can be guaranteed by using methods of Sarkissian et al. [59] and Doicu et al. [67]. For non-rigid shapes, the spheroidal T -matrix method in Ref. [56] or the approaches in the more recent work of Waterman [57] and Lim [58] can be applied to ensure the stability. However, those cases are not considered in the present study.

In the following, the corresponding comparisons were made with previous results using either the same theoretical method (T -matrix method) under plane wave illumination (a special case of Bessel beam with $\beta = 0^\circ$), or the partial-wave series expansion (PWSE) method under Bessel beam illumination. Panel (a) of Fig. 2 depicts the monostatic far-field backscattering form function of a highly elongated rigid immovable spheroid (with an aspect ratio $a/b = 10$) in the plane wave for end-on ($\theta_i = 0^\circ$) incidence with the increment of dimensionless frequency $\Delta(ka) = 0.02$. The solid lines are calculated using a MATLAB software package based on the present theoretical method, while the circles have been obtained

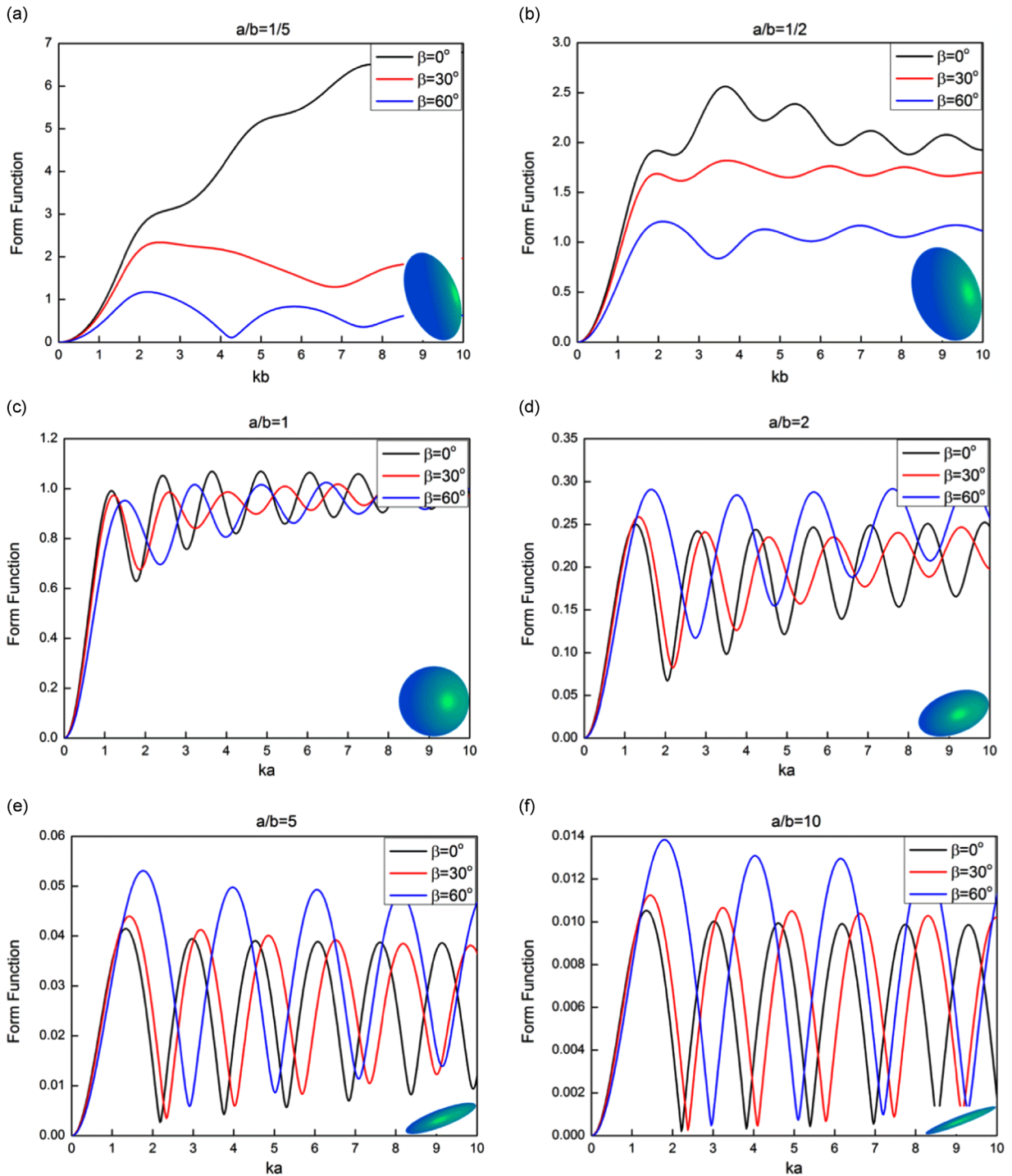


Fig. 3. The far-field backscattering form function modulus at end-on incidence $\theta_i = 0^\circ$ with different half-cone angles β of the Bessel beam versus the dimensionless frequency for rigid fixed (immovable) oblate spheroids [Panel (a), (b)], a rigid fixed sphere [Panel (c)], and rigid fixed prolate spheroids [Panel (d)–(f)]. The aspect ratio a/b is given on the top of each panel. The case where $\beta = 0^\circ$ corresponds to infinite plane waves.

using a commercial software (GetData) for the extraction of data from digital figures. Those correspond to previous results given in Fig. 37 (A) by Hackman [68]. As shown in the plots, the numerical results agree well with those of [68]. To further illustrate the effectiveness of the present method for an arbitrary incident direction, another test for a rigid prolate spheroid with an aspect ratio of $a/b = 2$ under the oblique incidence of plane wave with $\theta_i = 45^\circ$ is performed and results are displayed in panel (b) of Fig. 2. The results again match correctly with those given in Fig. 4 in Ref. [54]. As observed from the

plot, the two results show a complete agreement for the backscattering form function. In addition, the results of acoustic scattering under the Bessel beam illumination computed by the T -matrix method are all in good agreement with those obtained using the partial wave series expansion (PWSE) method presented in Fig. 7 of [23] for the bistatic scattering from a rigid sphere with $\beta = 30^\circ$ (see panel (c) of Fig. 2), and for the monostatic scattering from a rigid spheroid with $a/b = 3$, $\beta = 60^\circ$ in panel (F) of Fig. 4 of [32] (see panel (d) of Fig. 2). Consequently, based on the comparisons and discussions, it could be anticipated that the present method will be effective for scattering from rigid spheroid with large aspect ratio under the illumination of the zeroth-order Bessel beam.

3.2. Far-field scattering problems by rigid spheroids

In this part, a parametric study has been carried out for rigid spheroids at end-on incidence ($\theta_i = 0^\circ$) with particular emphasis on varying the half-cone angle β , dimensionless frequency and aspect ratios. The far-field backscattering form functions are calculated and the rigid spheroids considered here range from oblate to prolate with aspect ratios varying between 1/5 and 10. Particularly, it is necessary to keep the radii of the cross section perpendicular to the incident beam axis of both the oblate and prolate spheroids under the end-on incidence constant for comparisons, namely, the equatorial radius of the oblate spheroid is always equal to the polar radius of the prolate spheroid with different aspect ratios.

Panels (a)–(f) in Fig. 3 illustrate the far-field backscattering form function modulus with three values of the half-cone angle β of the Bessel beam ($\beta = 0^\circ$ (plane wave case), $30^\circ, 60^\circ$), and the rigid spheroid transforms from a flat to a highly elongated shape with aspect ratios $a/b = 1/5, 1/2, 1, 2, 5, 10$, respectively. In order to compare the results with previous data [32], the plots for oblate spheroids ($a < b$) are computed versus kb . As shown in these figures, it could be found that the backscattering form function modulus for oblate spheroids [Panel (a), (b)] decreases as β increases, while for the prolate spheroids [Panels (d)–(f)], the modulus increases as β increases. This may be explained using the highlight model [69]: the scatterer is characterized by a scattering highlight array (a group of corresponding scattering zones) in space which can be taken as sub-sources of individual partial-waves. For a rigid spheroid, the geometric highlight plays a dominant role in backscattering which is dependent on the radii of curvature at points of surface. The scattering intensity of highlight is enhanced as the radius of curvature increases. In the oblate spheroid case, when $\beta = 0^\circ$ (plane wave incidence), the far-field backscattering intensity are mainly attributed to the radiation of equivalent scattering zone at the end of minor axis ($r = a$) having a large radius of curvature, and this leads to a larger form function modulus comparing with those of the prolate spheroid. With the increase of the half-cone angle β , the highlight moves towards the endpoint of the major axis ($r = b$) with small curvature radius and at this time, the intensity of highlight will weaken, leading to a decrease in the magnitude of the backscattering form function. Similarly, in the prolate spheroid case, the highlight will shift from the end of the major axis ($r = a$) to that of the minor axis ($r = b$) as the half-cone angle β increases and the radius of curvature will become larger accordingly. It is obvious that the magnitude of the backscattering form function will increase with increasing half-cone angle β values from 0° to 60° . Furthermore, under illumination of Bessel beam with the same half-cone angle β , the far-field backscattering form function modulus exhibits a sustained downward trend under the transition from the oblate spheroid case [Panel (a)] to the prolate spheroid case [Panel (f)].

In particular, the quasi-periodic oscillations could be visibly observed in Fig. 3 when the backscattering form function modulus are plotted versus the dimensionless frequency ka or kb . The oscillations are enhanced for the prolate spheroid cases shown in Panels (d)–(f). The physical mechanisms of the quasi-periodic oscillations can be interpreted as the interference between the specular reflection and the Franz wave circumnavigating the spheroid in the surrounding fluid, as

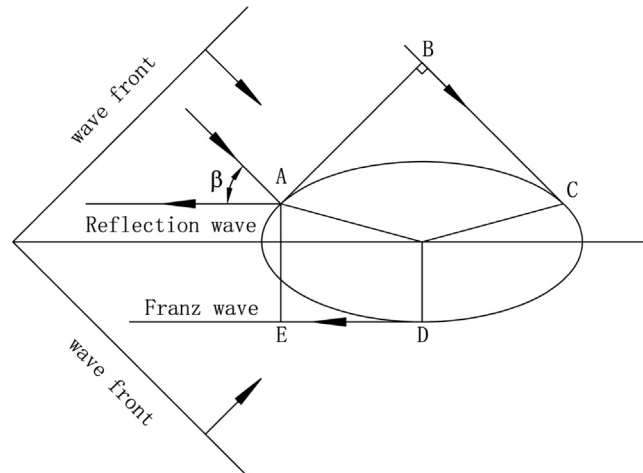


Fig. 4. The sketch of the geometric model of the Bessel beam scattering by a rigid fixed (immovable) prolate spheroid for end-on incidence $\theta_i = 0^\circ$ with the half-cone angle β .

Table 1

Comparison of the peak-to-peak intervals of the far-field backscattering form function modulus versus the dimensionless frequency for a rigid fixed prolate spheroid with three values of the aspect ratios $a/b = 2, 5, 10$, respectively, corresponding to half-cone angles $\beta = 0^\circ, 30^\circ, 60^\circ$.

Aspect ratio a/b	Half-cone angle β	Predicted by geometric model	Obtained from Fig. 3
2	0°	1.42	1.42
	30°	1.56	1.57
	60°	2.01	1.96
5	0°	1.51	1.54
	30°	1.62	1.67
	60°	2.14	2.12
10	0°	1.54	1.57
	30°	1.64	1.69
	60°	2.19	2.15

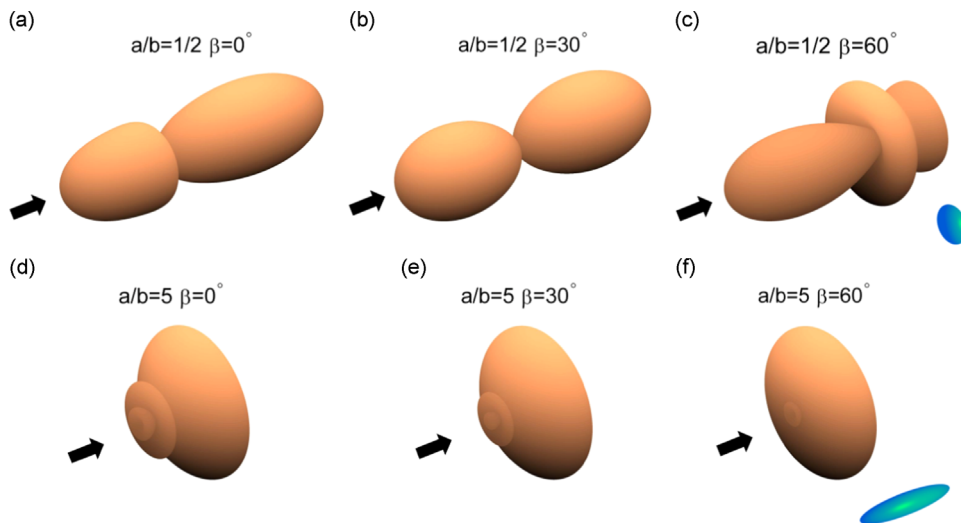


Fig. 5. The 3D far-field scattering directivity patterns at end-on incidence $\theta_i = 0^\circ$ with different half-cone angles β of the Bessel beam for a rigid oblate spheroid [Panels (a)–(c)] for $kb = 5$, and for a rigid prolate spheroid [Panels (d)–(f)] for $ka = 5$, respectively. The aspect ratios are given explicitly on the top of each panel. The arrows on the left-hand side of each panel indicate the direction of incidence of the Bessel beam.

shown by the geometric model in Fig. 4. It can be found that the specularly reflected wave starts at point A and reflects to the opposite direction of incident beam axis into the water, while the Franz wave propagates along \overline{BC} , \overline{CD} , and \overline{DE} , and then goes into the surrounding water parallel with the reflection wave. It should be noted that the geometric model is actually a generalization of the sphere case constructed in Fig. 4 of Ref. [23]. In the sphere case, the point on the surface (A1 in Ref. [23]) is easily to identify to produce a ray traveling antiparallel to the incident beam axis under the Bessel beam illumination with a specific half-cone angle, while the corresponding specular point on the spheroidal surface (A in Fig. 4) is not easy to identify since the center of curvature is not consistent with the geometric center of an arbitrary spheroid. As for the Franz wave, it gives weak scattering contributions to the backscattering because of radiation damping as the wave travels around the backside of the spheroid in a free field. It is interesting to note that the situations have been found where the Franz wave are the dominant scattering mechanism when the wave is partially reflected at a free surface [70], however, this will not be covered in the present study. As shown in Fig. 3, the peak-to-peak intervals in the backscattering form function plots differ from one another when the aspect ratio a/b of the spheroid changes. This phenomenon is due to the path difference between the specular and Franz wave contributions for spheroids with different aspect ratios. Furthermore, a comparison of the peak-to-peak intervals in the far-field backscattering form function plots versus the dimensionless frequency for a rigid fixed prolate spheroid is performed, with three values of the aspect ratios $a/b = 2, 5, 10$, respectively, with half-cone angles $\beta = 0^\circ, 30^\circ, 60^\circ$, as listed in Table 1. The dimensionless intervals are obtained throughout two different ways. The first is based on the analysis of the geometric model of the reflection and Franz waves for the prolate rigid spheroid [11], while the second is based on the direct measurement from the form function magnitude plots versus the dimensionless frequency displayed in Panels (d)–(f), respectively. As listed in Table 1, the peak-to-peak intervals predicted by the geometric model analysis reach a good agreement with the results obtained from Fig. 3.

To further explore the novel physical phenomenon of acoustic scattering by a rigid spheroid under the illumination of a zeroth-order Bessel beam, the 3D far-field scattering directivity patterns of an oblate and a prolate spheroids at end-on

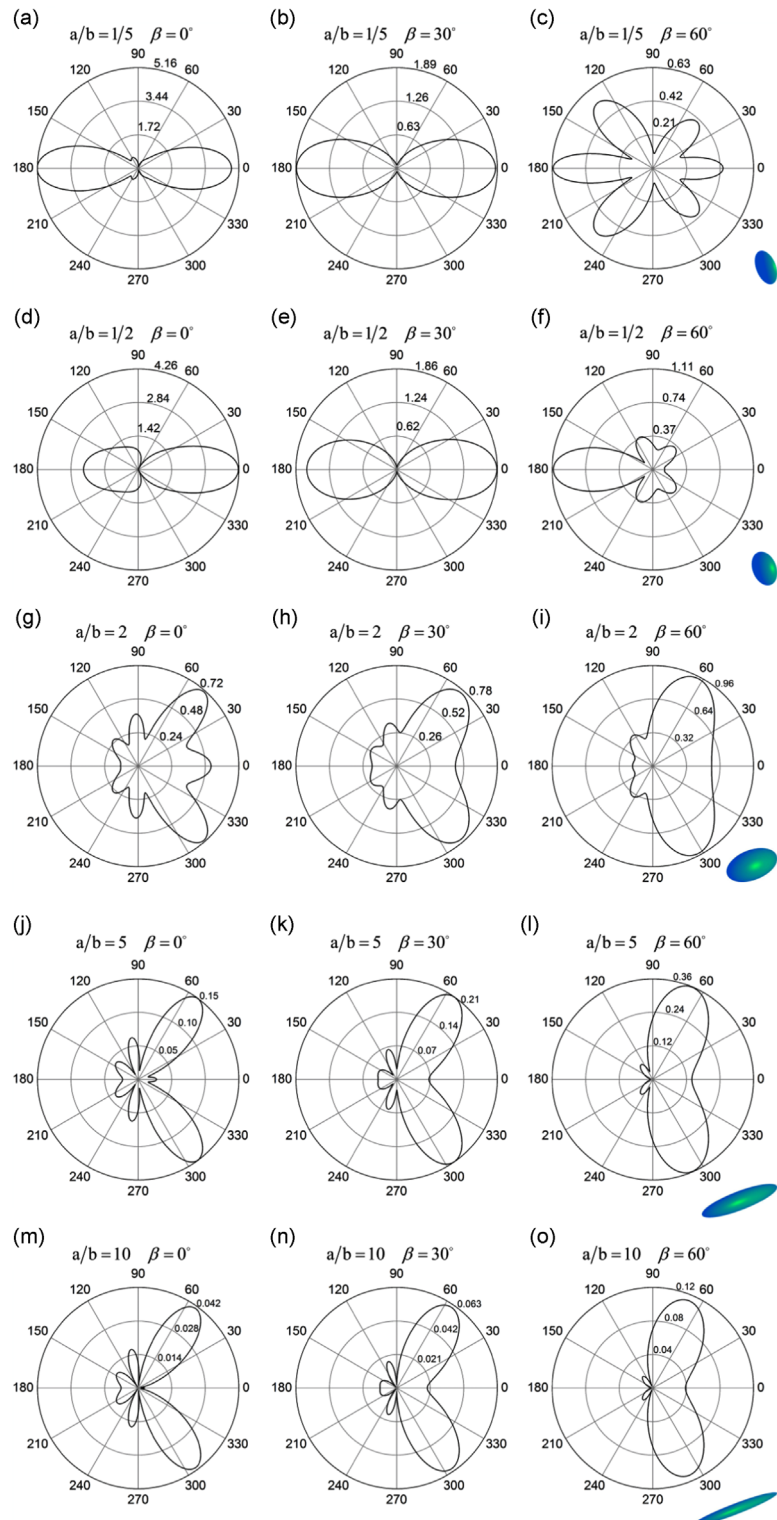


Fig. 6. The bistatic 2D far-field scattering polar diagrams at end-on incidence $\theta_i = 0^\circ$ with different half-cone angles β of the Bessel beam for a rigid oblate spheroid [Panels (a)-(f)] for $kb = 5$, and for a rigid prolate spheroid [Panels (g)-(o)] for $ka = 5$, respectively. The aspect ratios are given explicitly on the top of each panel.

incidence $\theta_i = 0^\circ$ are computed for the same half-cone angles selected previously, as shown in Fig. 5. Panels (a)–(c) depict the 3D directivity patterns for a rigid oblate spheroid with $a/b = 1/2$ for $kb = 5$ and the half-cone angles $\beta = 0^\circ, 30^\circ, 60^\circ$, respectively, which is given in detail on the top of each panel of Fig. 5. Panels (d)–(f) present the 3D directivity patterns for a rigid prolate spheroid with $a/b = 2$ for $ka = 5$ and the half-cone angles $\beta = 0^\circ, 30^\circ, 60^\circ$, respectively. The arrows on the left-

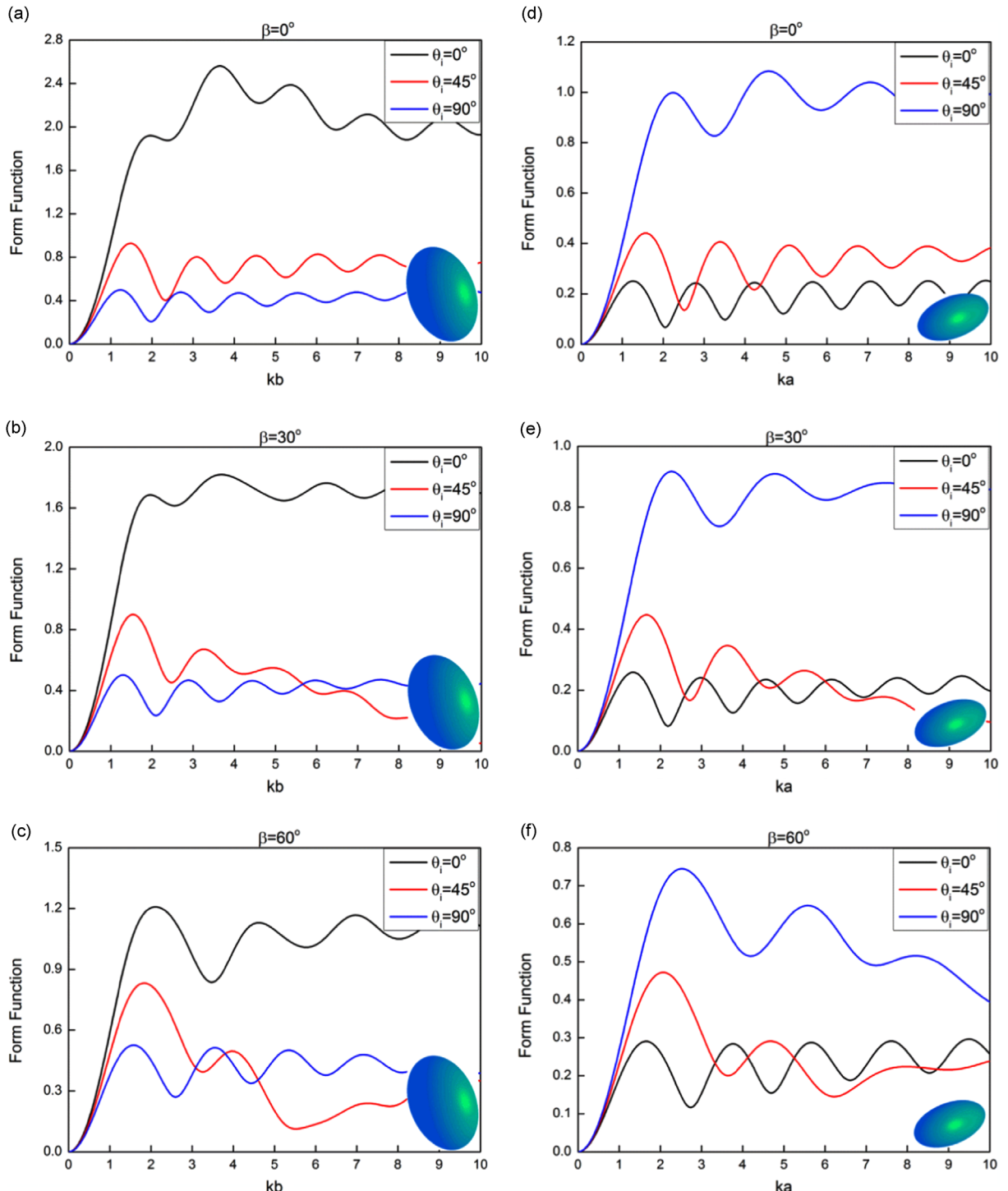


Fig. 7. The far-field backscattering form function modulus at arbitrary angles of incidence [$\theta_i = 0^\circ$ (end-on incidence), 45° , 90° (broadside incidence)] with different values of the half-cone angle β of the Bessel beam versus the dimensionless frequency for a rigid fixed oblate spheroid with an aspect ratio $a/b = 1/2$ [Panels (a)–(c)] and for a rigid fixed prolate spheroid with an aspect ratio $a/b = 2$ [Panels (d)–(f)].

hand side of each panel indicate the direction of the incident Bessel beam. By comparing with the oblate spheroid results shown in panels (a)–(c), it is obvious that the 3D directivity patterns for the prolate spheroids show significant differences, with particular emphasis on different values of β . Especially, for a highly elongated spheroid with an aspect ratio of $a/b = 5$, as shown in panels (d)–(f), the scattering in the shadow side ($\theta_s \in (0^\circ, 90^\circ) \cup (270^\circ, 360^\circ)$) of the spheroid plays a dominant role and the backscattering components almost vanishes. This phenomenon may be attributed to the extremely small radius of curvature at the end of spheroid, which leads to a weak backscattering intensity of highlight. To further make a quantitative analysis of the acoustic scattering from a rigid spheroid in Bessel beams, several bistatic 2D far-field scattering polar diagrams are presented in Fig. 6. Panels (a)–(f) depict the 2D polar diagrams for a rigid oblate spheroid with $a/b = 1/5$, $1/2$ for $kb = 5$ and the half-cone angles $\beta = 0^\circ, 30^\circ, 60^\circ$, respectively. Panels (g)–(o) gives the 2D polar diagrams for a rigid prolate

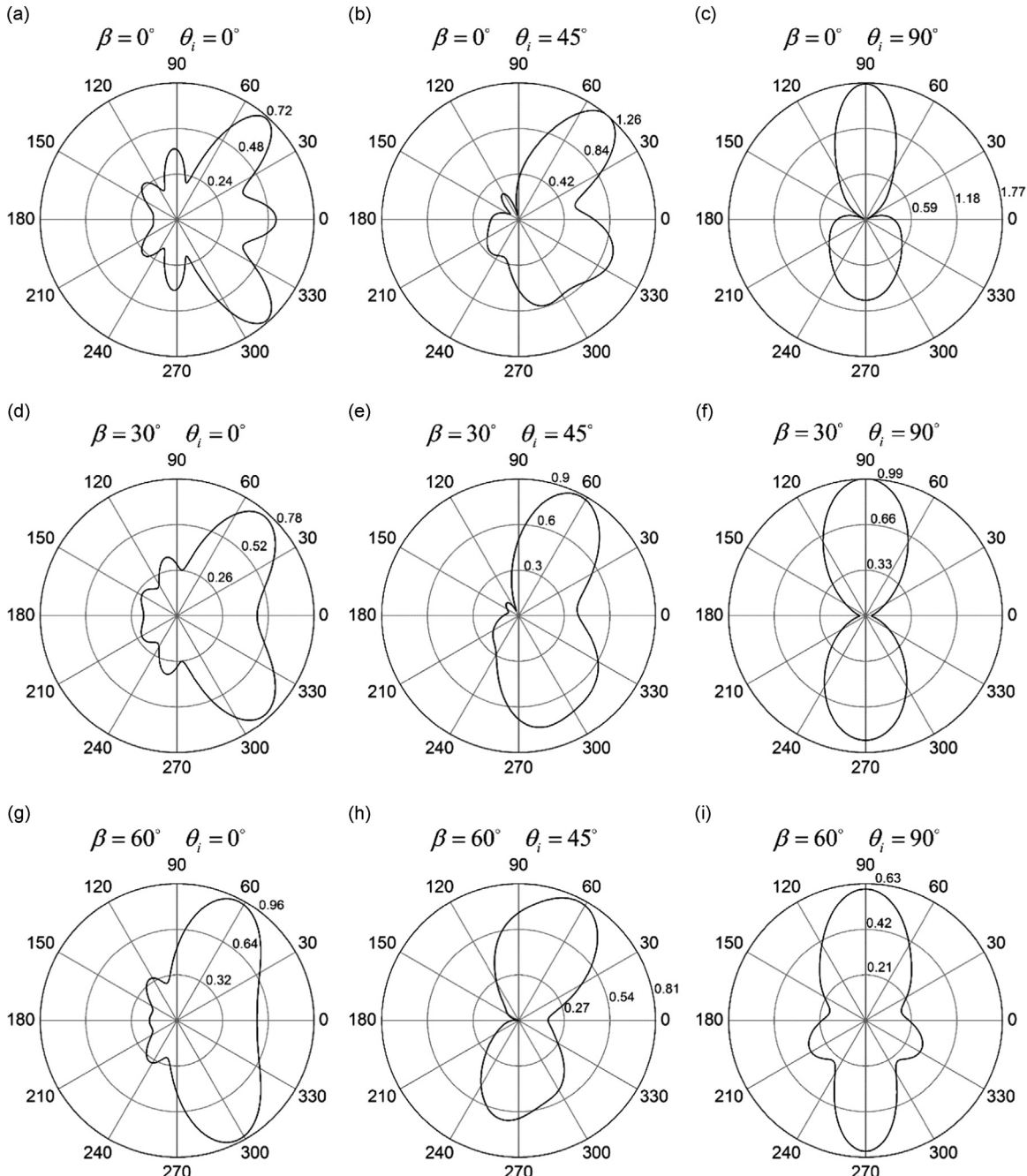


Fig. 8. The bistatic 2D far-field scattering polar diagrams for a rigid fixed prolate spheroid with an aspect ratio $a/b = 2$ for $ka = 5$, and the parameters of the incident axial angles θ_i and the half-cone angles β are the same as those used for Fig. 7. The half-cone angles $\beta = 0^\circ$ (panels (a)–(c)), 30° (panels (d)–(f)) and 60° (panels (g)–(i)), corresponding to the three rows with $\theta_i = 0^\circ, 45^\circ$, and 90° , respectively.

spheroid with $a/b = 2, 5, 10$ for $ka = 5$ with the same half-cone angles selected for the oblate spheroid cases. Again, the 2D polar diagrams of the oblate spheroid (panels (a)–(f)) show great differences from those of the prolate spheroid (panels (g)–(o)). Clearly, the half-cone angle has an obvious effect on the bistatic 2D far-field scattering polar diagrams for both the oblate and the prolate spheroids. In addition, it is interesting that the maximum values of the 2D polar diagrams for the oblate spheroid are always occurring in the forward scattering ($\theta_s = 0^\circ$) or backscattering ($\theta_s = 180^\circ$) directions under the end-on incidence, while the maximum values of the 2D polar diagrams for the prolate spheroid are not. For the rigid prolate spheroids with a constant aspect ratio, the maximum values have an increasing trend with the increase of the half-cone angle β , while the maximum value decreases with the half-cone angle β increases for the oblate spheroids with the same aspect ratio. Moreover, for the rigid prolate spheroids, the 2D polar diagrams patterns are exactly similar with the same half-cone angle for different aspect ratios, and the maximum values decrease with the aspect ratio of the rigid spheroid increases. This novel phenomenon may due to the fact that the scattering surface (a group of reradiated sub-sources) becomes smaller when the aspect ratio a/b increases since the polar radius a of the rigid prolate spheroid keeps constant.

3.3. Arbitrary angles of incidence

Several typical angles of incidence are selected, including $\theta_i = 0^\circ$ (end-on incidence), $\theta_i = 45^\circ$, and $\theta_i = 90^\circ$ (broadside incidence), with the same values of the half-cone angle β chosen previously. Panels (a)–(c) in Fig. 7 display the magnitude plots of the far-field backscattering form function versus the dimensionless frequency kb at three values of the incident axial angles θ_i for a rigid fixed oblate spheroid with an aspect ratio $a/b = 1/2$. Panels (d)–(f) in Fig. 7 correspond to the magnitude plots for the far-field backscattering form function versus the dimensionless frequency ka at three values of incident axial angles θ_i for a rigid fixed prolate spheroid with an aspect ratio $a/b = 2$, and the half-cone angles β are given on the top of each panel, respectively. Generally, for a fixed oblate spheroid with a specific β ($\theta_i = 0^\circ, 45^\circ$ or 90°) as displayed in panels (a)–(c), the backscattering form function modulus reduces as the incident axial angle increases. On the contrary, for a fixed prolate spheroid with a specific β , the backscattering form function modulus has an increasing trend as the incident axial angle increases, particularly in the low-medium frequency band, as shown in panels (d)–(f). These phenomena can be also explained using the highlight model as explicitly described before. For the oblate spheroid with a selected half-cone angle, the highlight will move towards to the endpoint of the major axis ($r = b$) with small curvature radius when the incident axial angle increases, leading to a decrease of the scattering intensity of the highlight. For the prolate spheroid with the same half-cone angle with the incident axial angle increasing, the highlight shifts from the end of the major axis ($r = a$) to the end of the minor axis ($r = b$). The curvature radius will become larger accordingly, and thus the scattering intensity of the highlight will increase.

To further investigate the physical mechanism of the scattering by a rigid spheroid in the field of an acoustic zeroth-order Bessel beam with arbitrary orientation, a rigid prolate spheroid with an aspect ratio $a/b = 1/2$ for $ka = 5$ is considered and several bistatic 2D far-field scattering polar diagrams are presented in Panels (a)–(i) of Fig. 8. Panels (a)–(i) display the polar magnitude plots of the far-field scattering form function with three discrete values of the incident axial angle θ_i with half-cone angles $\beta = 0^\circ, 30^\circ, 60^\circ$, respectively. It can be observed that the scattering polar diagrams are affected by both the half-cone angle β and the incident axial angle θ_i . Particularly, as shown in Panels (b), (e) and (h) of Fig. (8), the 2D polar patterns under the oblique incidence show the asymmetry, which are different from those of end-on and broadside incidence cases. Additionally, all the three 2D polar plots in Panels (a)–(c) are in line with those in Panels (d)–(f) of Fig. 3 in Ref. [71] for the plane wave incidence, respectively, which can further assert the correctness of the results.

4. Concluding remarks

In the present paper, the theoretical formalism using the T -matrix method to derive and compute the acoustic scattering by rigid oblate and prolate spheroids illuminated by an unbounded zeroth-order Bessel beam with arbitrary incidence is established. The proposed method is demonstrated to be capable of computing accurately the scattered field of extremely flat and highly elongated spheroids having an aspect ratio of 10:1 at arbitrary orientation. Based on the theoretical formulation derived above, a MATLAB software package is constructed and tested. It proved to be an effective numerical tool to tackle scattering problems for spheroids having large aspect ratios, in the field of a zeroth-order Bessel beam. Numerical computations are performed with particular emphasis on the half-cone angle β of Bessel beam, the dimensionless frequency, the aspect ratio a/b (=major axis/minor axis), as well as the angle of incidence θ_i . When encountering scattering problems by obstacles having complex geometries, and illuminated by a Bessel beam, the T -matrix method presents a useful and valuable tool along that direction of research.

Acknowledgments

This work is supported by the National Natural Science Foundation of China under Grant no. 51579112. The authors wish to thank Dr. Yongou Zhang and the anonymous reviewers for useful suggestions to improve the presentation of this manuscript.

References

- [1] J. Turunen, A. Vasara, A.T. Friberg, Holographic generation of diffraction-free beams, *Applied Optics* 27 (1988) 3959–3962.
- [2] Y. Lin, W. Seka, J.H. Eberly, H. Huang, D.L. Brown, Experimental investigation of Bessel beam characteristics, *Applied Optics* 31 (1992) 2708–2713.
- [3] J. Arlt, K. Dholakia, Generation of high-order Bessel beams by use of an axicon, *Optics Communications* 177 (2000) 297–301.
- [4] J. Chen, J. Ng, Z. Lin, C.T. Chan, Optical pulling force, *Nature Photonics* 5 (2011) 531–534.
- [5] R. Li, K.F. Ren, X. Han, Z. Wu, L. Guo, S. Gong, Analysis of radiation pressure force exerted on a biological cell induced by high-order Bessel beams using Debye series, *Journal of Quantitative Spectroscopy and Radiative Transfer* 126 (2013) 69–77.
- [6] Z. Chen, Y. Han, Z. Cui, X. Shi, Scattering of Bessel beam by a conducting spheroidal particle with dielectric coating, *Journal of Quantitative Spectroscopy and Radiative Transfer* 148 (2014) 197–202.
- [7] Z. Cui, Y. Han, Z. Chen, L. Han, Scattering of Bessel beam by arbitrarily shaped composite particles with core–shell structure, *Journal of Quantitative Spectroscopy and Radiative Transfer* 144 (2014) 108–116.
- [8] F.G. Mitri, R.X. Li, L.X. Guo, C.Y. Ding, Resonance scattering of a dielectric sphere illuminated by electromagnetic Bessel non-diffracting (vortex) beams with arbitrary incidence and selective polarizations, *Annals of Physics* 361 (2015) 120–147.
- [9] P.L. Marston, Axial radiation force of a Bessel beam on a sphere and direction reversal of the force, *The Journal of the Acoustical Society of America* 120 (2006) 3518–3524.
- [10] F.G. Mitri, Acoustic scattering of a high-order Bessel beam by an elastic sphere, *Annals of Physics* 323 (2008) 2840–2850.
- [11] W. Li, J. Li, Underwater acoustic scattering of a Bessel beam by rigid objects with arbitrary shapes using the T-matrix method, Proceedings of the OCEANS'12 MTS/IEEE, Hampton Roads, Virginia, October (2012), pp. 1–5.
- [12] Z. Gong, W. Li, Y. Chai, Acoustic resonance scattering of Bessel beam by elastic spheroids in water, Proceedings of the 6th International Conference on Computational Methods, Auckland, NZ, July (2015).
- [13] J. Durnin, Exact solutions for nondiffracting beams. I. The scalar theory, *Journal of the Optical Society of America A4* (1987) 651–654.
- [14] J. Durnin, J. Miceli, J.H. Eberly, Diffraction-free beams, *Physical Review Letters* 58 (1987) 1499–1501.
- [15] D.K. Hsu, F.J. Margetan, D.O. Thompson, Bessel beam ultrasonic transducer: Fabrication method and experimental results, *Applied Physics Letters* 55 (1989) 2066–2068.
- [16] R. Piestun, J. Shamir, Generalized propagation-invariant wave fields, *Journal of the Optical Society of America A15* (1998) 3039–3044.
- [17] Z. Bouchal, Nondiffracting optical beams: physical properties, experiments, and applications, *Czechoslovak Journal of Physics* 53 (2003) 537–578.
- [18] C. López-Mariscal, J.C. Gutiérrez-Vega, The generation of nondiffracting beams using inexpensive computer-generated holograms, *American Journal of Physics* 75 (2007) 36–42.
- [19] Z. Bouchal, J. Wagner, M. Chlup, Self-reconstruction of a distorted nondiffracting beam, *Optics Communications* 151 (1998) 207–211.
- [20] V. Garcés-Chavez, D. McGloin, H. Melville, W. Sibbett, K. Dholakia, Simultaneous micromanipulation in multiple planes using a self-reconstructing light beam, *Nature* 419 (2002) 145–147.
- [21] F.O. Fahrbach, P. Simon, A. Rohrbach, Microscopy with self-reconstructing beams, *Nature Photonics* 4 (2010) 780–785.
- [22] L. Zhang, P.L. Marston, Geometrical interpretation of negative radiation forces of acoustical Bessel beams on spheres, *Physical Review E* 84 (2011) 035601.
- [23] P.L. Marston, Scattering of a Bessel beam by a sphere, *Journal of the Acoustical Society of America* 121 (2007) 753–758.
- [24] P.L. Marston, Acoustic beam scattering and excitation of sphere resonance: Bessel beam example, *The Journal of the Acoustical Society of America* 122 (2007) 247–252.
- [25] F.G. Mitri, Acoustic beam interaction with a rigid sphere: The case of a first-order non-diffracting Bessel trigonometric beam, *Journal of Sound and Vibration* 330 (2011) 6053–6060.
- [26] F.G. Mitri, Z.E.A. Fellah, Instantaneous axial force of a high-order Bessel vortex beam of acoustic waves incident upon a rigid movable sphere, *Ultrasonics* 51 (2011) 719–724.
- [27] F.G. Mitri, G.T. Silva, Off-axial acoustic scattering of a high-order Bessel vortex beam by a rigid sphere, *Wave Motion* 48 (2011) 392–400.
- [28] F.G. Mitri, Equivalence of expressions for the acoustic scattering of a progressive high-order Bessel beam by an elastic sphere, *IEEE Transactions on Ultrasonics, Ferroelectrics, and Frequency Control* 56 (2009) 1100–1103.
- [29] F.G. Mitri, Interaction of a high-order Bessel beam with a submerged spherical ultrasound contrast agent shell–Scattering theory, *Ultrasonics* 50 (2010) 387–396.
- [30] F.G. Mitri, Generalized theory of resonance excitation by sound scattering from an elastic spherical shell in a nonviscous fluid, *IEEE Transactions on Ultrasonics, Ferroelectrics, and Frequency Control* 59 (2012) 1781–1790.
- [31] F.G. Mitri, Acoustic scattering of a Bessel vortex beam by a rigid fixed spheroid, *Annals of Physics* 363 (2015) 262–274.
- [32] F.G. Mitri, Axisymmetric scattering of an acoustical Bessel beam by a rigid fixed spheroid, *IEEE Transactions on Ultrasonics, Ferroelectrics, and Frequency Control* 62 (2015) 1809–1818.
- [33] F.G. Mitri, Acoustic radiation force on a sphere in standing and quasi-standing zero-order Bessel beam tweezers, *Annals of Physics* 323 (2008) 1604–1620.
- [34] F.G. Mitri, Langevin acoustic radiation force of a high-order Bessel beam on a rigid sphere, *IEEE Transactions on Ultrasonics, Ferroelectrics, and Frequency Control* 56 (2009) 1059–1064.
- [35] F.G. Mitri, Negative axial radiation force on a fluid and elastic spheres illuminated by a high-order Bessel beam of progressive waves, *Journal of Physics A: Mathematical and Theoretical* 42 (2009) 245202.
- [36] G.T. Silva, J.H. Lopes, F.G. Mitri, Off-axial acoustic radiation force of repulsor and tractor bessel beams on a sphere, *IEEE Transactions on Ultrasonics, Ferroelectrics, and Frequency Control* 60 (2013) 1207–1212.
- [37] F.G. Mitri, Acoustic radiation force on oblate and prolate spheroids in Bessel beams, *Wave Motion* 57 (2015) 231–238.
- [38] F.G. Mitri, Acoustical pulling force on rigid spheroids in single Bessel vortex tractor beams, *EPL, Europhysics Letters* <http://dx.doi.org/10.1209/0295-5075/112/34002>.
- [39] G.T. Silva, An expression for the radiation force exerted by an acoustic beam with arbitrary wavefront (L), *The Journal of the Acoustical Society of America* 130 (2011) 3541–3544.
- [40] W. Li, J. Li, Z.X. Gong, Study on underwater acoustic scattering of a Bessel beam by rigid objects with arbitrary shapes, *Acta Physica Sinica* <http://dx.doi.org/10.7498/aps.64.154305>.
- [41] L. Flax, G.C. Gaunaud, H. Überall, Theory of resonance scattering, *Physical Acoustics* 15 (1981) 191–294.
- [42] T.B.A. Senior, The scattering from acoustically hard and soft prolate spheroids for axial incidence, *Canadian Journal of Physics* 44 (1966) 655–667.

- [43] J.P. Barton, N.L. Wolff, H. Zhang, C. Tarawneh, Near-field calculations for a rigid spheroid with an arbitrary incident acoustic field, *The Journal of the Acoustical Society of America* 113 (2003) 1216–1222.
- [44] M.F. Iskander, A. Lakhtakia, C.H. Durney, A new procedure for improving the solution stability and extending the frequency range of the EBCM, *IEEE Transactions on Antennas and Propagation* 31 (1983) 317–324.
- [45] A. Lakhtakia, V.K. Varadan, V.V. Varadan, Iterative extended boundary condition method for scattering by objects of high aspect ratios, *The Journal of the Acoustical Society of America* 76 (1984) 906–912.
- [46] S. Wang, Finite-difference time-domain approach to underwater acoustic scattering problems, *The Journal of the Acoustical Society of America* 99 (1996) 1924–1931.
- [47] F. Ihlenburg, *Finite Element Analysis of Acoustic Scattering*, Springer, New York, 1998.
- [48] J.A. Roumeliotis, A.D. Kotsis, G. Kolezas, Acoustic scattering by an impenetrable spheroid, *Acoustical Physics* 53 (2007) 436–447.
- [49] M.F. Werby, S.A. Chin-Bing, Some numerical techniques and their use in the extension of T-matrix and null-field approaches to scattering, *Computers Mathematics with Applications* 11 (1985) 717–731.
- [50] P.C. Waterman, Matrix formulation of electromagnetic scattering, *Proceedings of the IEEE* 53 (1965) 805–812.
- [51] P.C. Waterman, Symmetry, unitarity, and geometry in electromagnetic scattering, *Physical Review D* 3 (1971) 825–839.
- [52] H. Überall, L.R. Dragonette, L. Flax, Relation between creeping waves and normal modes of vibration of a curved body, *The Journal of the Acoustical Society of America* 61 (1977) 711–715.
- [53] L. Flax, V.K. Varadan, V.V. Varadan, Scattering of an obliquely incident acoustic wave by an infinite cylinder, *The Journal of the Acoustical Society of America* 68 (1980) 1832–1835.
- [54] V.K. Varadan, V.V. Varadan, L.R. Dragonette, L. Flax, Computation of rigid body scattering by prolate spheroids using the T-matrix approach, *The Journal of the Acoustical Society of America* 71 (1982) 22–25.
- [55] L.H. Green, Acoustic resonance scattering by large aspect-ratio solid targets, *IEEE Journal of Oceanic Engineering* 81 (1987) 368–379.
- [56] R.H. Hackman, D.G. Todoroff, An application of the spheroidal coordinate-based transition matrix: The acoustic scattering from high aspect ratio solids, *The Journal of the Acoustical Society of America* 78 (1985) 1058–1071.
- [57] P.C. Waterman, T-matrix methods in acoustic scattering, *The Journal of the Acoustical Society of America* 125 (2009) 42–51.
- [58] R. Lim, A more stable transition matrix for acoustic target scattering by elongated objects, *The Journal of the Acoustical Society of America* 138 (2015) 2266–2278.
- [59] A. Sarkissian, C.F. Gaumond, L.R. Dragonette, T-matrix implementation of forward scattering from rigid structures, *The Journal of the Acoustical Society of America* 94 (1993) 3448–3453.
- [60] P.C. Waterman, New formulation of acoustic scattering, *The Journal of the Acoustical Society of America* 45 (1969) 1417–1429.
- [61] W. Li, *Inverse Reconstruction of Underwater Objects Based on Acoustic Scattering* (Ph.D. thesis), National University of Singapore, Singapore, 2004.
- [62] W. Li, Y. Zhao, T. Zhang, J. Liu, Computation and analysis of the acoustic scattering field from submerged rigid objects, *Technical Acoustics* 26 (2007) 844–849.
- [63] J.A. Stratton, *Electromagnetic Theory*, John Wiley & Sons, New Jersey, 2007.
- [64] W.G. Neubauer, R.H. Vogt, L.R. Dragonette, Acoustic reflection from elastic spheres. I. Steady-state signals, *The Journal of the Acoustical Society of America* 55 (1974) 1123–1129.
- [65] L.R. Dragonette, et al., Acoustic reflection from elastic spheres and rigid spheres and spheroids. II. Transient analysis, *The Journal of the Acoustical Society of America* 55 (1974) 1130–1137.
- [66] L. Flax, L.R. Dragonette, H. Überall, Theory of elastic resonance excitation by sound scattering, *The Journal of the Acoustical Society of America* 63 (1978) 723–731.
- [67] A. Doicu, Y. Eremin, T. Wriedt, *Acoustic and Electromagnetic Scattering Analysis Using Discrete Sources*, Academic Press, New York, 2000.
- [68] R.H. Hackman, Acoustic scattering from elastic solids, *Physical Acoustics* 22 (1993) 1–194.
- [69] W.L. Tang, Highlight model of echoes from sonar targets, *Chinese Journal of Acoustics* 13 (1994) 131–140, <http://dx.doi.org/10.15949/j.cnki.0217-9776.1994.02.004>.
- [70] G.C. Eastland, P.L. Marston, Enhanced backscattering in water by partially exposed cylinders at free surfaces associated with an acoustic Franz wave, *The Journal of the Acoustical Society of America* 135 (2014) 2489–2492.
- [71] F.G. Mitri, Acoustic scattering of a cylindrical quasi-Gaussian beam with arbitrary incidence focused on a rigid elliptical cylinder, *Journal of Applied Physics* <http://dx.doi.org/10.1063/1.4935275>.